Evaluation of instability in fractured rock masses using numerical analysis methods: Effects of fracture geometry and loading direction

Article *in* Journal of Geophysical Research Atmospheres · November 2001

DOI: 10.1029/2001JB000311

CITATIONS
34

READS
47

2 authors, including:

David J. Sanderson
University of Southampton
200 PUBLICATIONS **8,170** CITATIONS

SEE PROFILE

JOURNAL OF GEOPHYSICAL RESEARCH, VOL. 106, NO. B11, PAGES 26,671–26,687, NOVEMBER 10, 2001

Evaluation of instability in fractured rock masses using numerical analysis methods: Effects of fracture geometry and loading direction

Xing Zhang and David J. Sanderson

T. H. Huxley School of Environment, Earth Sciences and Engineering, Imperial College of Sciences, Technology and Medicines, London, England, United Kingdom

Abstract. Numerical modeling, using two-dimensional distinct element methods, is used to examine the effect of stress on the stability of a fractured rock mass. The critical stress state depends on the differential stress, mean stress, and fluid pressure and is represented by a surface which bounds all stable stress states. By examining the critical stress states under different loading conditions it is possible to define the stability/instability in terms of the far-field differential stress and effective mean stress. Thus the strength of fractured rock can be represented by a macroscopic frictional component (μ_z) and a cohesion (C_z), which differ from the corresponding parameters for individual fractures. A series of simulations are used to examine the effects of fracture network geometry, such as fracture density, fracture length, and fracture network anisotropy, on the instability strength. A steady decrease in equivalent frictional strength (μ_e) with increasing fracture density was found. For the same fracture density, rock masses with fewer, but larger, fractures had lower instability strength. As networks became more anisotropic, the orientation of the fractures in relation to the loading direction had a considerable impact on the instability strength and deformation pattern. The effects of loading direction in relation to fracture set orientation have been examined for two fracture networks with different anisotropy coefficients. Where the directions of the principal stresses were parallel to the fracture sets, extensional deformation was observed. Otherwise, dilational shear deformation modes develop, within which sliding, opening, and block rotation occur.

1. Introduction

A range of phenomena from earthquakes to hydrocarbon migration and hydrothermal ore deposits are directly related to faulting, fluid flow, and their interaction. Direct evidence for this interaction includes natural and reservoir-induced seismicity, earthquakes triggered by fluid injection, forced oil recovery, and waste disposal [*Healy et al.*, 1968; *Raleigh et al.*, 1976; *Das and Scholz*, 1981; *Talwani and Acree*, 1985].

In many investigations it is necessary use the fracture geometry to characterize rock masses and their bulk properties [e.g., *Dershowitz and Einstein,* 1988]. Fractures of all sizes have a major effect on the physics of the upper crust, such as the mechanical, hydraulic, thermal, and seismic properties. The deformability and permeability do not follow a smooth, progressive change at all scales of space and time in the upper crust. Instead, they may increase nonlinearly with increasing fracture density, fracture length, orientation, roughness and connectivity [e.g., *Zhang and Sanderson* 1994].

Most work on fractures and fluid flow treats the fracture network as a passive system, with fractures having a fixed transmissivity. Recently, it has been recognized that flow is greatly enhanced in critically stressed fractures, usually identified on the basis of their orientation with respect to the in situ stress field [*Barton et al.,* 1995] or by coupled modeling of flow and deformation [*Zhang and Sanderson,* 1997; *Sanderson and Zhang,* 1999]. It is this stress sensitivity that is examined in this paper.

The localization of deformation in fractures and shear zones is of fundamental importance to many topics in the earth sciences [*Cox*, 1999; *Sanderson and Zhang*, 1999]. The onset of localized deformation is a critical point phenomenon at which the mechanical and hydraulic behavior of the system suddenly changes, usually involving a huge increase in hydraulic conductivity and deformation [*Zhang and Sanderson*, 1997; *Sanderson and Zhang*, 1999]. Laboratory tests, field observation, numerical analysis, and case studies demonstrate that the deformation and strength of fracture rock masses are largely influenced by fractures at all scales [*Lajtai*, 1969; *Hoek and Brown*, 1980; *Einstein et al.,* 1983; *Gerrard,* 1986; *Zhang*, 1993]. For example, fracture interconnections allow the development of macroscopic deformation [*Chelidze,* 1986] when fracture density increases during tectonic processes.

Rock masses may experience very different loading histories, involving both the magnitude of the principal stresses and their orientation in relation to the fracture sets. Human activity may alter the stress state in a fractured rock mass. For example, the fluid pressure, and hence effective stress, may be changed by injection or extraction of fluid [*Harper and Last*, 1990; *Santarelli et al.*, 1992; *Zhang et al.*, 1999a]. Engineering practice has demonstrated that a regional stress release exists around an underground excavation, and this may cause

Paper number 2001JB000311.
0148-0227/01/2001JB000311$09.00

changes in permeability and stability [*Jaeger and Cook*, 1979; *Hudson*, 1987; *Pusch*, 1989; *Zhang et al.*, 1999b].

In this paper, numerical modeling methods are used to simulate the deformation of fractured rock masses. The critical stress state at which instability occurs was found by monitoring the displacements and unbalanced force within the system. The critical state is that at which the rock mass becomes unstable by the action of a small increment of stress. The effects of fracture network geometry and loading direction on the instability strength and deformation behavior have been investigated for a series of simulated fracture networks, which allow different features of the fracture network geometry and applied stresses to be assessed.

2. Stress States Surrounding Fractured Rock Masses

Since most shallow seismicity is associated with slip along preexisting fractures [*Rummel et al.*, 1986; *Spicak et al.*, 1986], the instability of the upper crust is mainly controlled by the slip of fractures. For a single fracture the shear strength may be expressed by the Coulomb failure criterion

$$\tau = (\sigma_n - P_f) \tan \phi + C, \quad (1)$$

where τ is the shear stress along the fracture, σ_n is the normal stress acting across the fracture surface, P_f is the fluid pressure, ϕ is the fraction angle, and C is the cohesion.

It is difficult to determine the stability of a system of fractures by an analysis using the Coulomb criterion due to the variation of local stress state within the rock mass. More importantly, failure locally within the system will change the stress and may either promote or suppress deformation in surrounding areas. This is now widely recognized in seismic hazard studies [e.g., *Scholz*, 1990; *Harris*, 1998].

The stress state surrounding an equilibrium system of fractured rocks is expressed with the principal effective stresses (σ_1' and σ_3') and orientation (θ), where the Coulomb failure stress (CFS) is

$$\mathrm{CFS} = f(\sigma_1',\ \sigma_3',\ \theta). \quad (2)$$

A change in the Coulomb failure stress, ΔCFS, can be obtained by any change in the principal stresses:

$$\Delta\mathrm{CFS} = f(\Delta\sigma_1',\ \Delta\sigma_3',\ \theta). \quad (3)$$

If ΔCFS > 0, the region becomes closer to instability, whereas if ΔCFS < 0, it moves farther from instability. For some examples, spatial patterns of static stress changes calculated for mainshocks correlate well with spatial patterns of aftershocks [e.g., *Reasenberg and Simpson*, 1992; *Harris*, 1998; *Toda et al.*, 1998]. An important question is when will the stress state in a fractured rock mass attain the critical state at which a small positive change in ΔCFS is likely to trigger instability.

3. Determination of Critical Stress States Using Numerical Methods

The distinct element method was implemented using the UDEC code (Universal Distinct Element Code) [*Cundall et al.*, 1978]. This incorporates a Mohr-Coulomb model for the intact blocks, a Coulomb–slip model and stress-related aperture for the fractures, and the cubic law for fluid flow through the fractures. The rock blocks generally behave elastically and may be divided internally into triangular elements and stresses calculated by finite difference methods. The Coulomb-slip model incorporates several important features of the physical response of fractures. In the normal direction, the stress displacement relation is assumed to be linear and governed by the stiffness k_n such that

$$\Delta\sigma_n' = -k_n \Delta u_n, \quad (4)$$

where $\Delta\sigma_n'$ is the effective normal stress increment and Δu_n is the normal displacement increment. Similarly, the response in shear is controlled by a constant shear stiffness k_s. The shear stress τ is limited by a combination of cohesion C and friction angle ϕ (equation (1)). Thus, if $|\tau| \leq \tau_{max}$, then

$$\Delta\tau = -k_s \Delta u^e_s, \quad (5)$$

or else, if $|\tau| \geq \tau_{max}$, slip occurs, and then

$$\tau_s = \mathrm{sign}\ (\Delta u_s)\ \tau_{max}, \quad (6)$$

where Δu^e_s is the elastic component of the incremental shear displacement and Δu_s is the total incremental shear displacement. The models allow large finite displacement and deformations with the UDEC code recognizing new contact geometries that may arise during the deformation [*Cundall et al.*, 1978].

A simulated two-dimensional fracture network of 10 x 10 m (Figure 1) was used to represent a horizontal plane within a rock mass containing vertical fractures (Figure 2). The network in Figure 1 will be used to explain the procedures for determining the critical stress. The fractures are well connected, with a density of 7.85 m^{-1} (defined as total fracture length per unit area) and an average length of 1.15 m. The properties of the fractures have a dominant effect on the total deformation behavior with the effective elastic modulus of the rock mass being determined by the properties of the fractures and the intact rock (Table 1).

The rock has a density of 2600 kg m^{-3} and is subject to an overburden stress, σ_v = 13 MPa, corresponding to a depth of

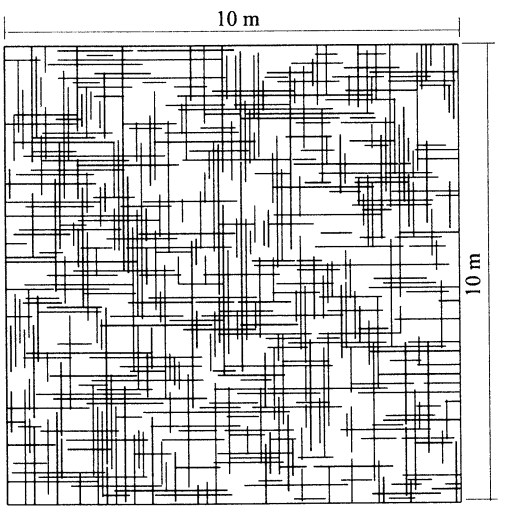

Figure 1. The simulated fractured rock mass of 10 m by 10 m used in the initial analysis. This consists of two orthogonal sets of fractures with a density of 7.85 m^{-1} and an average length of 1.15 m.

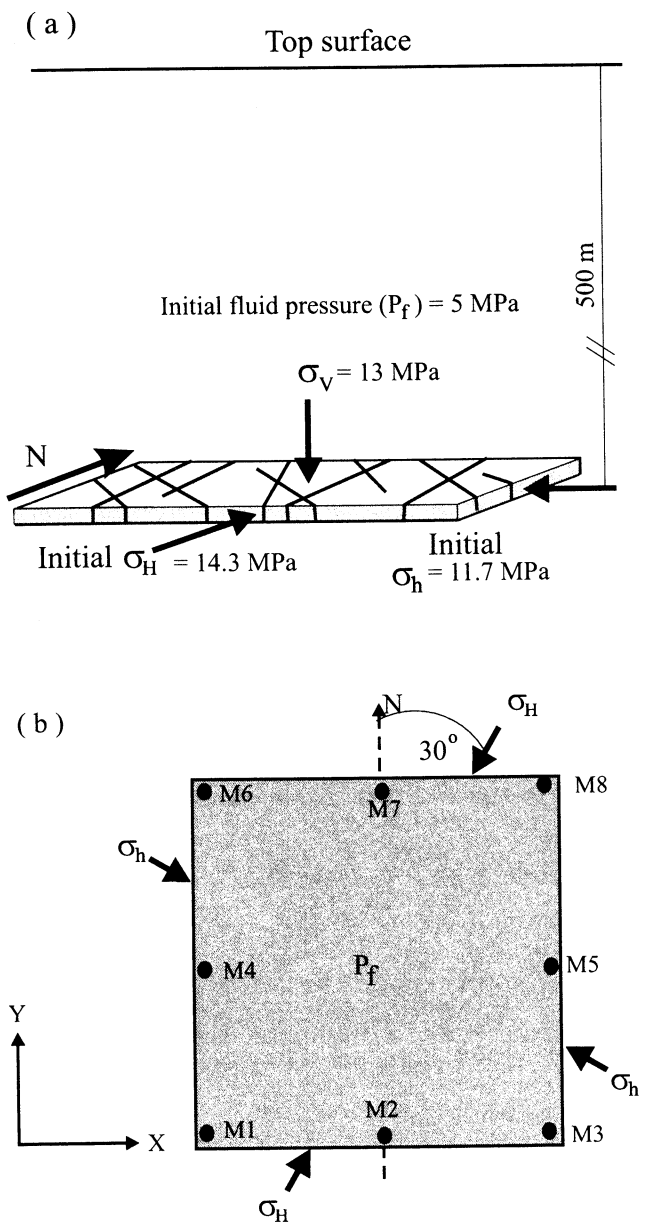

Figure 2. (a) Initial stresses selected in modelling with an overburden (σ_V) of 13 MPa, a major horizontal principal stress (σ_H) of 14.3 MPa and a minor horizontal principal stress (σ_h) of 11.7 MPa. (b) Loading directions of principal horizontal stresses (σ_H) and location of monitoring system (M1-M8).

~500 m. The initial major and minor horizontal principal stresses, σ_H and σ_h were set at 14.3 and 11.7 MPa, respectively (Figure 2a), with a hydrostatic fluid pressure of 5 MPa. The directions of the principal stresses and monitors for displacement are shown in Figure 2b. The rock mass was allowed to reach an equilibrium state under the action of the initial stress field. During the equilibration, the system was brought to a stable state, indicated by the displacements at the eight monitoring points (Figure 2b) approaching steady values.

The model was then loaded by increasing the differential stress or the fluid pressure or decreasing the mean stress or some combination of these. Initially, an increment of 1 MPa in differential stress was used with the fluid pressure and the mean stress unchanged; smaller changes were used in searching for the critical state.

After application of a ΔCFS increment, displacements of the monitoring points and unbalanced forces exist. Prior to instability the displacements rapidly attain a constant value (Figures 3a and 3b, right) and the magnitude of the unbalanced forces approaches zero (Figure 3c). At the critical state (differential stress, q = 10.6 MPa), the system becomes unstable as indicated by accelerating displacements (Figures 3a and 3b, left) and an increase in unbalanced forces (Figure 3c).

The behavior of the system does not change smoothly with increasing stress. Initially, the shear displacements along fractures are fairly uniformly distributed through the network (Figure 4a). Approaching the critical state, the maximum shear displacement is ~6 mm, and displacement is localized on a few fractures (Figure 4b). At the critical state, further increase in ΔCFS produces instability and shear displacements >30 mm are highly localized within a throughgoing shear zone (Figure 4c). This shear zone comprises a complex system of linked fractures with high shear and opening displacements. The direction of the shear zone is at an angle $\beta = 23°$ to the major horizontal principal stress σ_H (Figure 4c).

In addition to shear displacement, dilational deformation also developed during the movements (Figure 5). Initially apertures are small and fairly uniformly distributed through the network (Figure 5a) and the resultant flow would be low and diffuse. At the critical state the linked dilational shear zone contains fractures with very large apertures (>8 mm, see Figure 5c) that form jogs between fractures with high shear displacement. These are likely to lead to a sudden change of fluid flow from diffuse flow through fractures to highly localized flow often at fracture intersections [*Sanderson and Zhang*, 1999].

An increase in conductivity and permeability of rock samples prior to failure has been observed in laboratory experiments by *Patterson* [1978]. *Zhang et al.* [1994] report an increase in permeability of up to 2 orders of magnitude during

Table 1. Parameters Used in UDEC modeling

Model Parameters	Value	Units
	Rock Properties	
Density	2600	kg m^{-3}
Shear modulus	10	GPa
Bulk modulus	30	GPa
Tensile strength	4	MPa
Cohesion	10	MPa
Friction angle	30	degree
	Fracture Properties	
Shear stiffness	50	GPa m^{-1}
Normal stiffness	100	GPa m^{-1}
Tensile strength	0	MPa
Cohesion	0	MPa
Friction angle	30	degree
Dilation angle	5	degree
Residual aperture	0.02	mm
Zero stress aperture	0.5	mm
	Fluid Properties	
Density	1000	kg m^{-3}
Viscosity	0.00035	Pa s

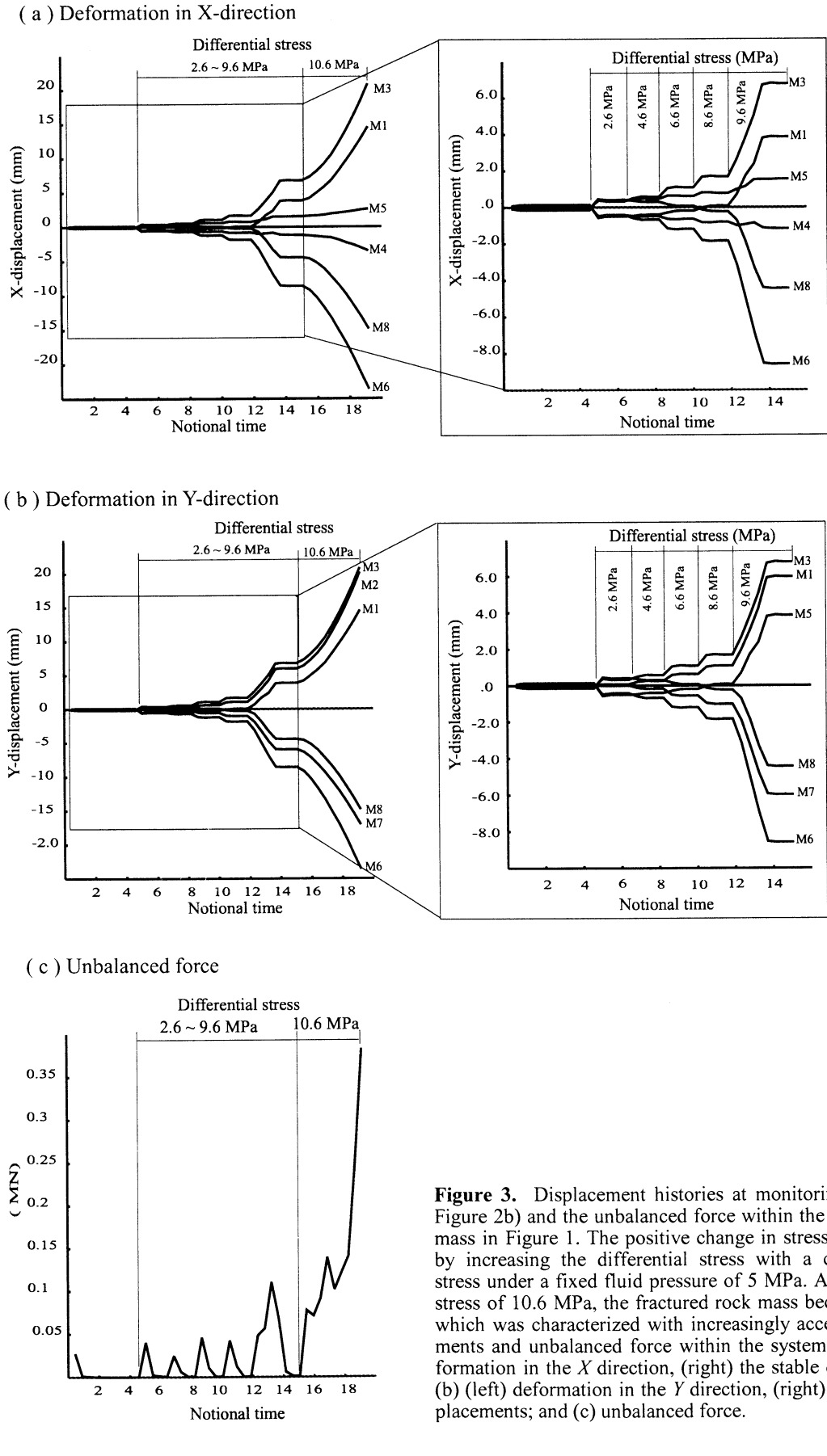

Figure 3. Displacement histories at monitoring points (see Figure 2b) and the unbalanced force within the fractured rock mass in Figure 1. The positive change in stress was achieved by increasing the differential stress with a constant mean stress under a fixed fluid pressure of 5 MPa. At a differential stress of 10.6 MPa, the fractured rock mass became unstable, which was characterized with increasingly accelerated movements and unbalanced force within the system. (a) (left) Deformation in the *X* direction, (right) the stable displacements; (b) (left) deformation in the *Y* direction, (right) the stable displacements; and (c) unbalanced force.

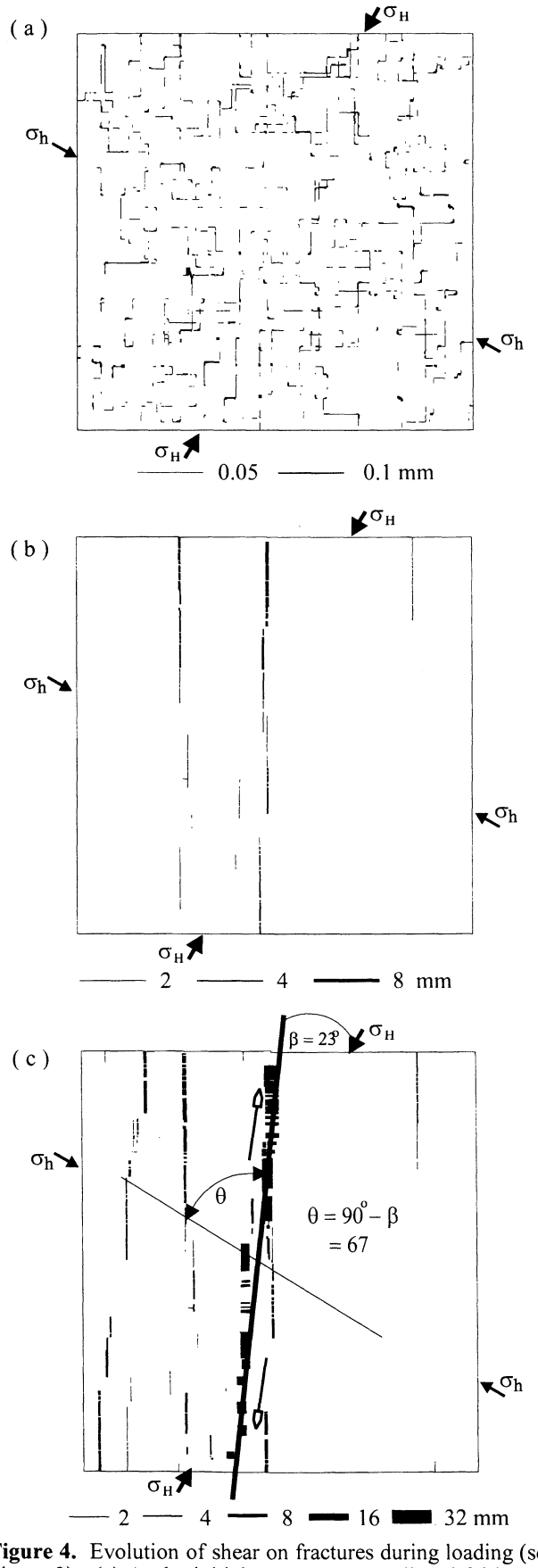

Figure 4. Evolution of shear on fractures during loading (see Figure 3). (a) At the initial stress state, small and fairly uniformly distributed shear. (b) At the precritical stress state, the increased shear displacement beginning to localize. (c) At the critical stress state, greatly increased shear displacement and a linked dilational shear zone formed at ~23° to σ_H.

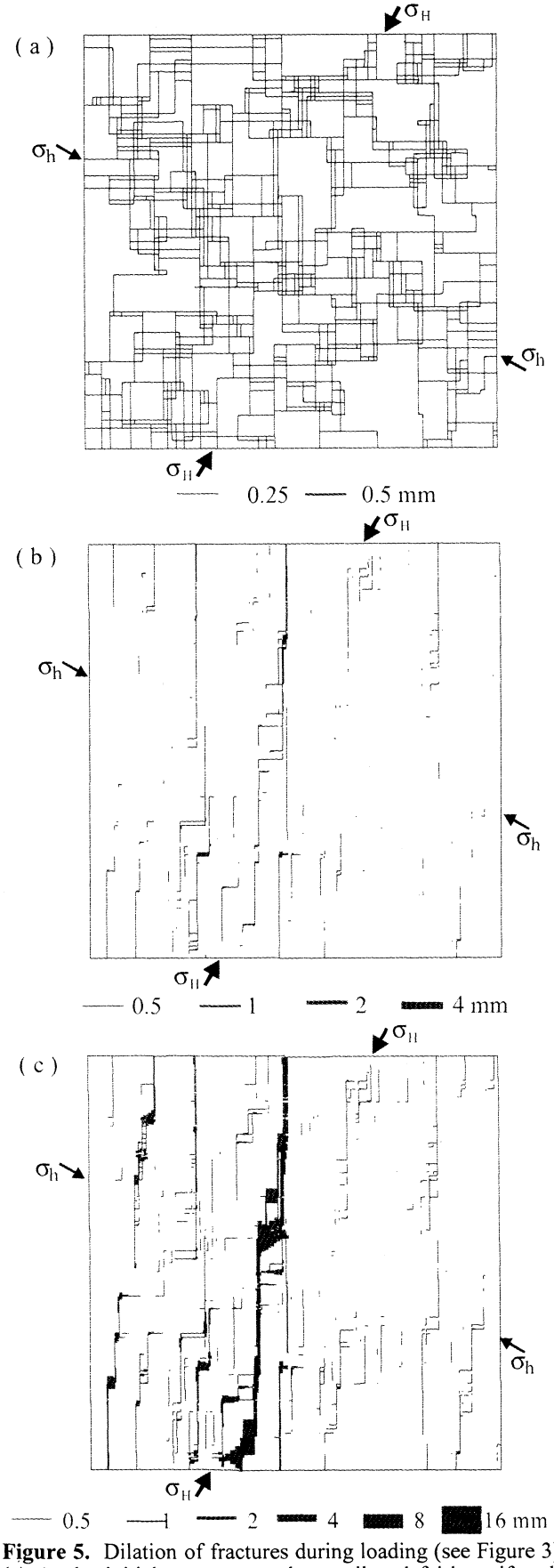

Figure 5. Dilation of fractures during loading (see Figure 3). (a) At the initial stress state, the small and fairly uniformly distributed dilation. (b) At the precritical stress state, considerably increased dilation particularly at jogs on fractures with higher shear. (c) At the critical stress state, short dilational jogs, developed as part of a dilational shear zone.

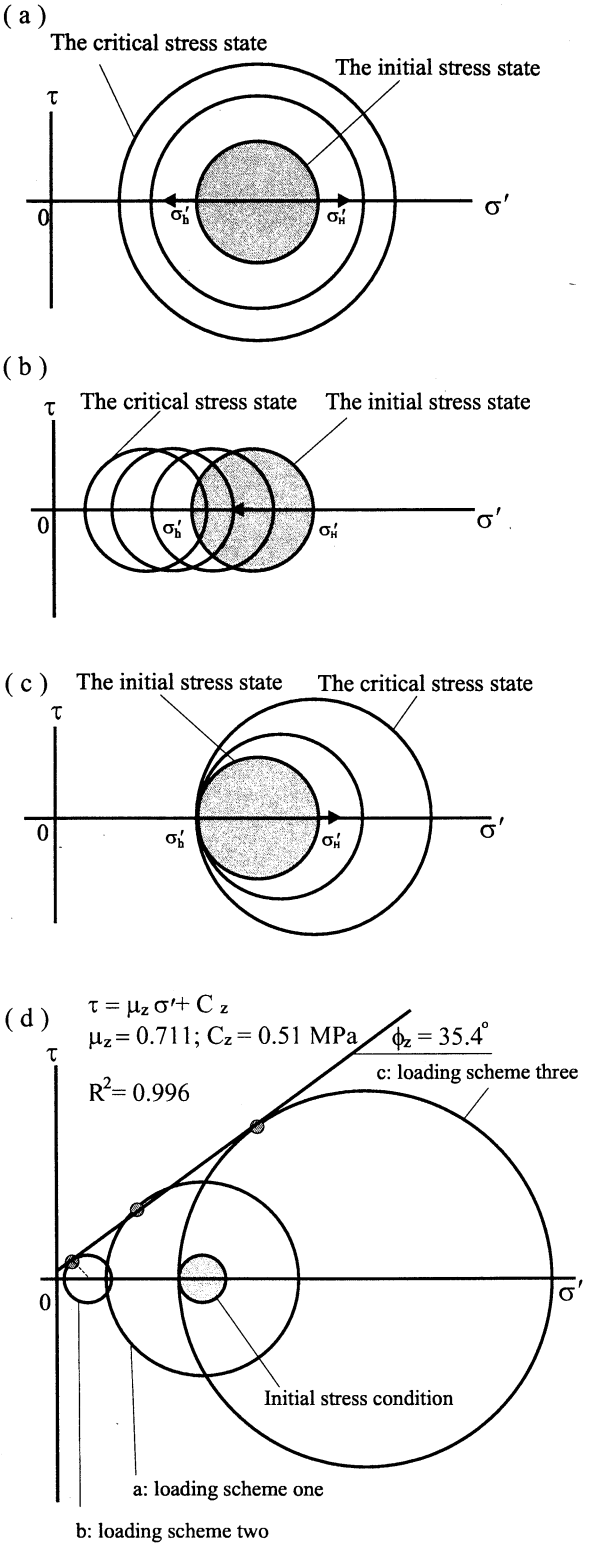

Figure 6. Schematic illustration of Mohr circles for the three loading schemes used in the modelling. (a) Loading scheme 1. The mean stress and fluid pressure are kept constant and the differential stress increased by increasing σ_H and decreasing σ_h. (b) Loading scheme 2. The fluid pressure is increased, keeping σ_H and σ_h (and hence differential stress) constant with the mean stress decreasing. (c) Loading scheme 3. The major principal stress (σ_H) is increased so the differential and mean stresses also increase. (d) Instability strength defined by the Mohr circles at the three critical stress states, which produce a failure envelope with a frictional coefficient of 0.73 and cohesion of 0.4 MPa.

deformation of Carrara marble, which they attribute to microcrack development.

The critical phenomenon may also be explained by a mechanical percolation model [*Chelidze*, 1986; *Reuschle*, 1998]. Rock failure may be understood on a microscopic scale by a statistical consideration of microcracking within a specimen. The resulting macroscopic failure is highly localized at the critical stage even though the microdamage may be described by a percolation model and is characterized by nonlocalized features.

4. Instability Strength of Fractured Rock Masses

In the previous model a positive change in stress, ΔCFS, was obtained by increasing the differential stress while the mean stress and fluid pressure remain constant (Figure 6a). A positive ΔCFS could also be obtained by altering other stress components, such as the fluid pressure (loading scheme 2, Figure 6b) and the maximum horizontal stresses (loading scheme 3, Figure 6c). These produce three different critical stress states as follows: scheme 1, fluid pressure of 5 MPa, differential stress of 10.6 MPa, abd mean stress of 13 MPa; scheme 2, fluid pressure of 11.3 MPa, differential stress of 2.6 MPa, and mean stress of 13 MPa; scheme 3, fluid pressure of 5 MPa, differential stress of 20.6 MPa, and mean stress of 22 MPa.

These are specific cases of all possible states of stresses, which may be understood by reference to a state boundary surface (Figure 7) plotted with axes $q = \sigma_H - \sigma_h$ (differential stress), $p = (\sigma_H + \sigma_h)/2$ (mean stress), and P_f (fluid pressure). The importance of the state boundary surface is that it represents a surface below which the rock mass is stable and above which it is unstable on application of a small positive ΔCFS.

It is common in the literature to state the Coulomb failure stress change without detailing the assumptions regarding fluid behavior. Mohr circles can be used to represent the critical stress state, as shown in Figure 6d, where the failure surface is tangential to each Mohr circle. In this case, the strength of the fractured rock mass can be described by a friction coefficient ($\mu_z = \tan\varphi_z = 0.73$; $\varphi_z = 36°$) and a cohesion ($C_z = 0.4$ MPa). Note that the frictional coefficient is slightly higher than that used for individual fractures in the modeling, and that a higher effective cohesion developes (see Table 1).

For intact rock the shear strength is generally described by a friction coefficient and a cohesion [e.g., *Bernaix*, 1969; *Jaeger and Cook*, 1979]. For a smooth, single fracture, shear strength can be defined by a friction coefficient. For fractured rocks and single fractures with rough surfaces, laboratory tests show that shear strength can be described by a friction angle (plus a dilation angle) where the confining stress was low [e.g., *Byerlee*, 1978; *Hung and Lee,* 1990; *Bro*, 1992] but requires both a friction angle and cohesion where the confining stress was high [e.g., *Byerlee*, 1978; *Bro*, 1992] or where fractures are not throughgoing [e.g., *Hung and Lee,* 1990]. Similarly, both a friction angle and cohesion are necessary to describe the strength of large volumes of fractured rock masses [e.g., *Vlokh et al.*, 1987; 1990].

In the present study, no single fracture spans the model and failure occurs by the production of a zone comprising numerous sliding and opening fractures in different directions (Figures 4 and 5). Analysis of the resulting failure stresses implies a small cohesion (C_z) (see Figures 6 and 9). Thus the instabil-

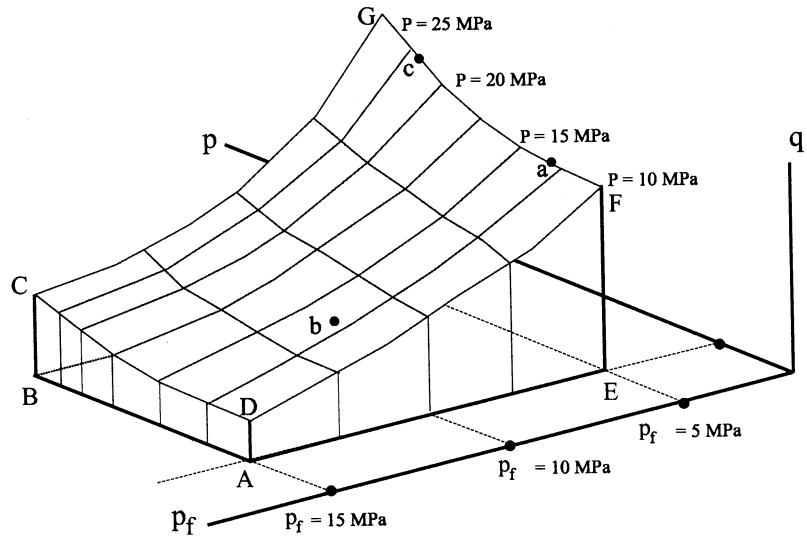

Figure 7. State boundary surface with axes q, p, and P_f where $q = \sigma_H - \sigma_h$ is the differential stress, $p = (\sigma_H + \sigma_h)/2$ is the mean stress, and P_f the fluid pressure. Line GF represents all possible states of instability at the hydrostatic pressure, and line CD represents them at a higher fluid pressure. Lines DF and CG are critical state lines at a low and high mean stress, respectively. The points a (q = 10.6, MPa, p = 13 MPa, P_f = 5 MPa), b (q = 2.6, MPa, p = 13 MPa, P_f = 11.3 MPa) and c (q = 20.6, MPa, p = 22 MPa, P_f = 5 MPa) correspond to the critical stress states for the model in Figure 1, under the three loading schemes in Figure 6.

ity strength of the rock mass as a whole can not be described adequately by the Coulomb failure criterion for a single fracture.

In theory, for a homogenous continuum the failure surface makes an angle of $\beta = (90^\circ - \varphi)/2$ with the major principal stress. In this modeling (Figure 6d) the predicted failure surface had an angle of $\beta = 27.3^\circ$ ($45^\circ - \varphi_z/2$). At lower effective mean stress, the angle of β was smaller (23°, Figures 4c and 8a) than that under a higher effective mean stress (28°, Figure8b). The associated dilational deformation is also different. Under low effective mean stress, the shear zones have significant dilational jogs or pull-aparts (Figures 5a and 8c), whereas under a high effective mean stress these are much less developed (Figure 8d).

To further examine the instability behavior, two more initial boundary conditions were used, corresponding to greater depths of 1000 m and 1500 m. Again, the directions of the resulting shear zones at different depths were slightly different. At a depth of 1000 m, $\beta = 24^\circ$ (Figure 8e), whereas at a depth 1500 m, $\beta = 28^\circ$ (Figure 8f).

The three initial boundary conditions, corresponding to depths of 500, 1000, and 1500 m, where each subject to the three loading schemes, giving a total of nine critical stress states. The Mohr circles at these nine critical stress states indicate an instability strength envelope, as shown in Figure 9. The frictional coefficient (μ_z) was estimated to have a value of 0.73 (friction angle, $\varphi_z = 36^\circ$), and the cohesion (C_z) was ~0.4 MPa. These estimates are in agreement with field data observed by *Barton et al.* [1995] and *Zoback et al.* [1996], for which friction coefficients between 0.6 and 0.9 are reported.

5. Determination of Normalized Stability

In practice, it is difficult to determine the shear and normal stress along a potential shear zone because the zone is made up from an array of linked fractures. On the other hand, the differential stress (q) and effective mean stress (p') are easy to estimate at the critical state in the model. By plotting $q/2$ against p', an equivalent friction coefficient (μ_e) and an equivalent cohesion (C_e) may be determined from the best fit straight line (Figure 9). The equivalent friction coefficient μ_e = 0.58 is less than μ_z = 0.73 and provides an alternative estimate of the instability strength.

Using plots of q against p', it is possible to determine the stability under various stress conditions. For example, the stability of the fractured rock mass in Figure 1 at various depths between 500 and 2000 m is shown in Figure 10. In this case, σ_H was selected to be 1.2 times the vertical stress, and σ_h was selected to be 0.65 times the vertical stress. For each depth the stresses assuming hydrostatic pressure and 1.35 times hydrostatic pressure are plotted. Under hydrostatic pressure the rock mass is stable at depths between 500 m and 2000 m. However, at 1.35 time hydrostatic it is unstable at depths greater than ~1000 m.

Another way to compare the stability of a fractured rock is to define a normalized stability factor (S_n) (Figure 11). For a specific stress state (p' and q) an associated, critical stress state (p_c' and q_c) could be determined according to the instability strength line at which the two stress states had the shortest distance. Then S_n can be obtained by the ratio of the two slopes:

$$S_n = S_c(q_c / p_c') / S(q / p') = \tan \alpha_c / \tan \alpha . \quad (7)$$

For a stress state within the unstable domain, $S_{n1} < 1$, whereas in the stable domain, $S_{n2} > 1$.

On the basis of the data in Figure10 the stability factor S_n at various depths has been calculated (Figure 12a). At a depth of 500 m the rock mass had S_n = 1.51 under the hydrostatic pressure and S_n = 1.19 under 1.35 times hydrostatic pressure. On the other hand, at a depth of 2000 m the rock mass was stable with S_n = 1.24 at hydrostatic pressure but unstable with S_n = 0.94 at 1.35 times the hydrostatic pressure. Also, the degree of stability of the fractured rock mass was very different under different in situ stress (Figure 12b).

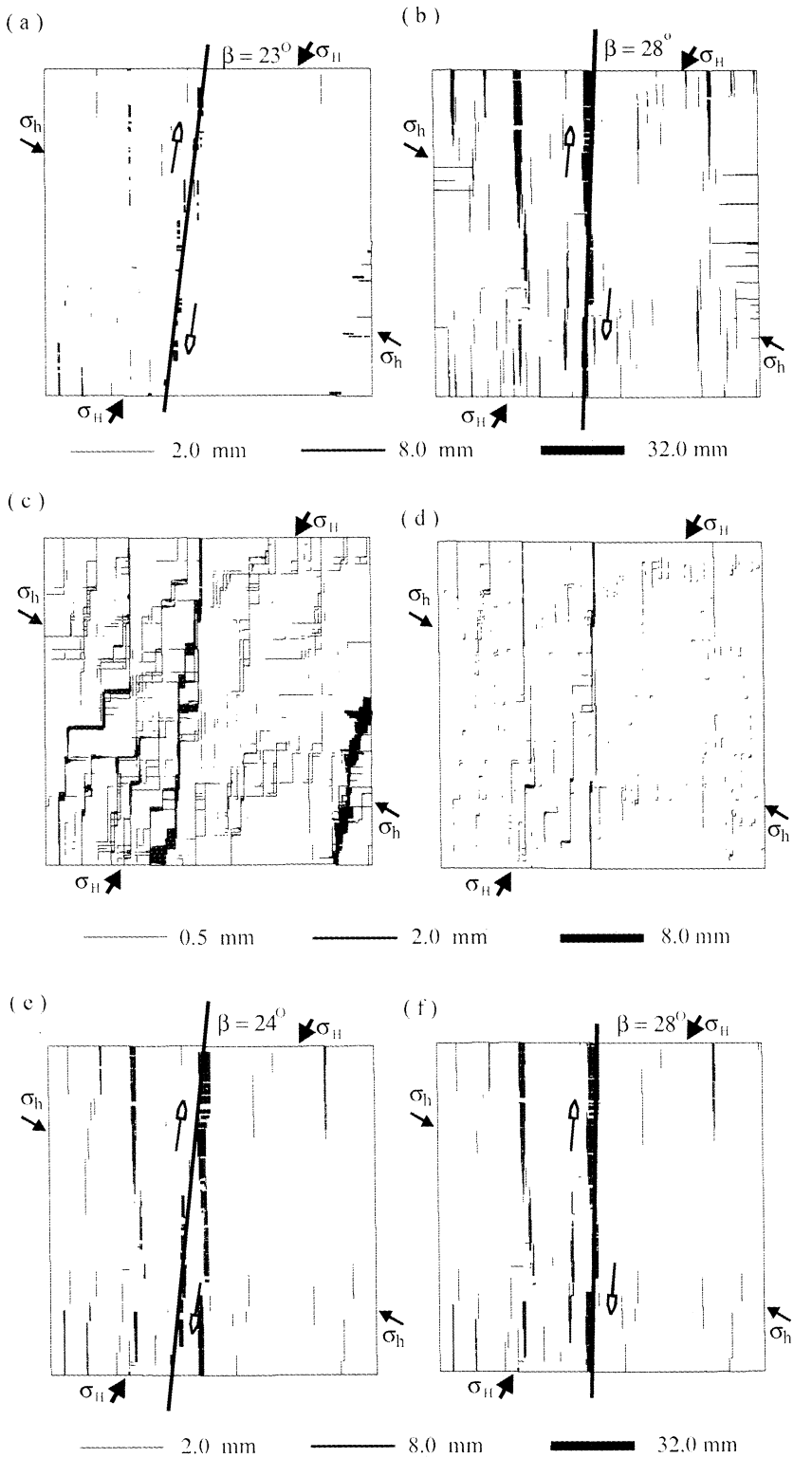

Figure 8. Shear displacements developed at the critical stress states with different loading schemes at a depth of 500 m. (a) Loading scheme 2 (p' = 1.7 MPa and q = 9.6 MPa) with a shear zone at 23° to σ_H. (b) Loading scheme 3 (p' = 17 MPa and q = 20.6 MPa) with a shear zone at 28° to σ_H. Dilational deformation developed at the critical stress states as in (c) Figure 8a and (d) Figure 8b. Shear zones developed at the critical stress states at different depths with loading scheme 1. (e) At a depth of 1000 m (p' = 14.05 MPa, q = 17.3 MPa), with a shear zone at 24° to σ_H. (f) At a depth of 1500 (p' = 21.08 MPa, q = 26.45 MPa), with a shear zone at 28° to σ_H.

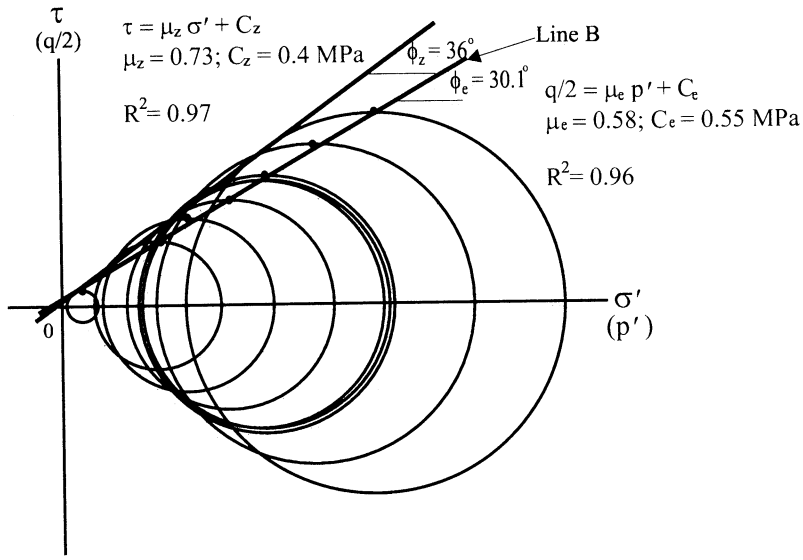

Figure 9. Instability strength defined by Mohr circles at the critical stress states at depths of 500, 1000, and 1500 m, with three loading schemes. The Coulomb failure envelop (A) corresponds to a frictional coefficient of 0.73 and cohesion of 0.4 MPa. The line B represents the maximum shear stress ($q/2$) at various mean effective stresses (p') and defines the equivalent friction coefficient $\mu_e = 0.58$ and equivalent cohesion $C_e = 0.55$ MPa.

6. Effects of Fracture Network Geometry

Simulated fracture networks allow a systematic study of the interplay and relative importance of the two key factors: fracture network geometry and applied stress state. Fracture networks have been simulated within a square of 10 x 10 m. All models comprise two sets of parallel, orthogonal fractures. The fracture density, fracture length, and anisotropy of fracture networks are systematically varied. The modeling involves procedures similar to those described by *Sanderson and Zhang* [1999, in press], but here the instability is examined in terms of the equivalent frictional coefficient μ_e.

Fractures were generated sequentially, with the coordinates of their centers randomly selected from a uniform distribution. A procedure of self-avoiding generation was used, such that new fractures were selected only if they were located at a minimum distance to previously generated fractures. The minimum distance can be varied but was set at 50 mm (i.e., 0.5% of the size of the square) in this study. Trace lengths were sampled from a power law distribution where the num-

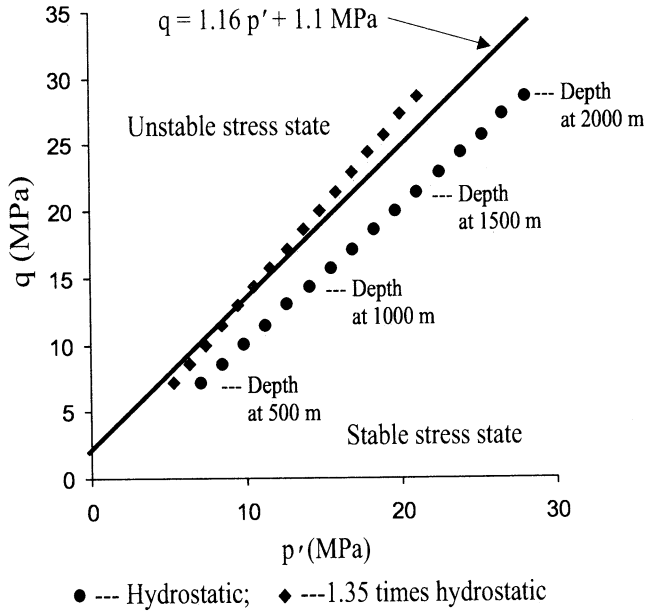

Figure 10. Plot of differential stress (q) against mean effective stress (p') with increasing depth for model in Figure 1 at hydrostatic (circles) and 1.35 x hydrostatic (diamonds) fluid pressures. The solid line represents the instability strength determined in Figure 9.

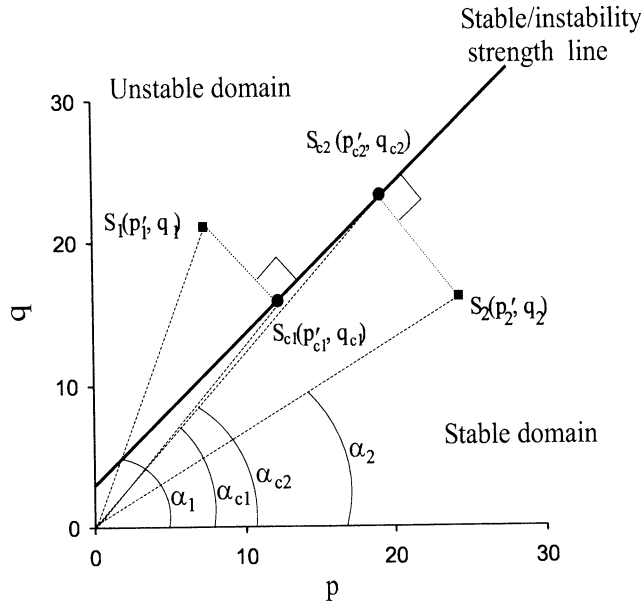

Figure 11. Definition of normalised stability factor S_n from a plot of $q/2$ against p' (for further explanation see text).

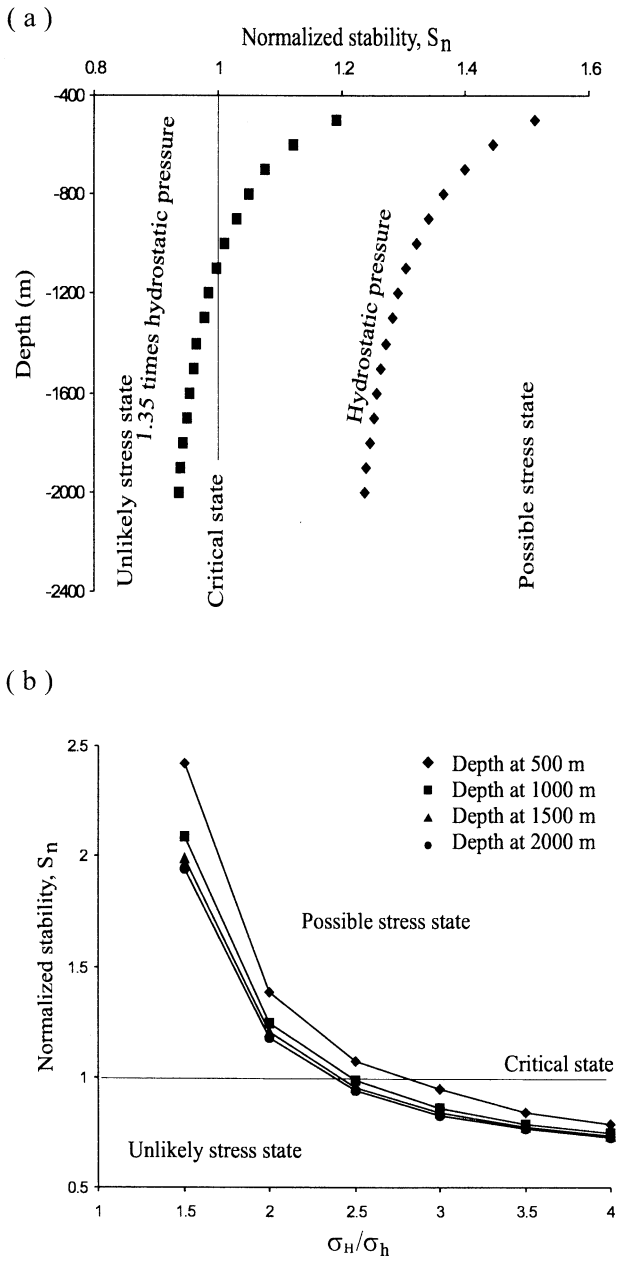

Figure 12. Prediction of the degree of stability of the fractured rock mass (as in Figure 1) according to the normalized stability factor. (a) Normalized stability factor at depth between 500 and 2000 m under different fluid pressures (diamonds hydrostatic pressure; squares 1.35 hydrostatic pressure). (b) Normalized stability factor plotted against principal stress ratios for different depths.

ber of fractures (N) of length (L) had a form $N \propto aL^E$. The exponent (E) was set to 1.2 and the fracture trace length varied from a fixed upper limit of 2.5 m to a lower limit of between 0.1 m and 2 m. For each simulated facture network, three loading schemes were used, as shown in Figures 6a-6c; initially, the loading direction was fixed at $\sigma_H = 30^\circ$.

6.1. Fracture Density

In this group of simulations both fracture sets are equally represented and have an average fracture length of 1.15 m (range 0.5 and 2.5 m). The overall density was varied between 4.3 and 11.6 m^{-1}, the former (Figure 13a) corresponding to the percolation threshold, below which the fracture network consisted of individual fractures and locally connected clusters, with no spanning (or critical) cluster [e.g., *Stauffer and Aharony*, 1991; *Zhang and Sanderson*, 1994, 1998]. At the higher fracture density of 11.6 m^{-1} (Figure 13b) the fractured rock was highly fragmented.

Figures 13c and 13d show the dilation at the critical stress state for two rock masses with different fracture densities under loading scheme 2. At low fracture density, displacement developed along only a few paths and dilational jogs are large (Figure13c). The critical stress state required a high fluid pressure of 16 MPa. At higher fracture density, most fractures contribute to the spanning cluster, and hence there are more potential slip paths. However, only one dilational shear zone formed, which followed a fairly straight path with small jogs (Figure 13d). The critical state is reached at a lower fluid pressure of 11.5 MPa.

Figure 13e shows that the equivalent frictional strength μ_e decreases from 0.74 to 0.44, as fracture density increases from 4.3 to 11.6 m^{-1}. This confirms results from experimental study of deformability of a percolating system [e.g., *Benguigui*, 1984], who showed that the deformability increased with increasing the porosity.

6.2. Fracture Length

In this group of simulations the fracture density was constant at 7.85 m^{-1}, and the average length of both sets of fractures varied. This was achieved by setting an upper limit of 2.5 m and selecting lower limits at 0.1, 0.2, 0.5, 1, 1.5, and 2 m to produce a variation in average fracture length between 0.61 and 2.11 m.

For shorter fracture lengths a higher fluid pressure (14 MPa) was needed to reach the critical stress state and the shear zone had large jogs due to the short fractures (Figure 14a). For longer average lengths the critical fluid pressure was lower (12 MPa), and the shear zones were relatively straight (Figure 14b). The equivalent frictional strength (μ_e) decreases from 0.67 to 0.47 (Figure 14c).

6.3. Anisotropy

In this group of simulations the total fracture density was kept constant at 7.85 m^{-1}, but the average fracture lengths in the x and y direction varied independently between 0.1 and 1 m. This produced an anisotropy, in which the ratio of fracture densities of the two sets [*Zhang and Sanderson*, 1995] varied between 0.3 and 3.35 (Figure 15).

As the anisotropy varies, the deformation style and instability strength differ significantly. At lower anisotropy (0.3, Figure 15a), longer fractures at 60° to σ_H link to produce dilational shear zones at 45°-50° to σ_H, with large jogs (see Figures 15c and 2b). At the critical stress state the fluid pressure was 16 MPa. At high anisotropy (3.35, Figure 15b), the longer fractures are at 30° to σ_H and the dilational shear zones form at a relatively small angle (26°) to σ_H (Figure 15d). In this case, the fluid pressure was 11.4 MPa at the critical stress state. The equivalent frictional strength, μ_e, decreased somewhat, from 0.69 to 0.5 with increasing anisotropy (Figure 15e). Thus, as networks become more anisotropic, the orientation of the fractures in relation to the loading direction has a considerable impact on the critical stress state. Because of the

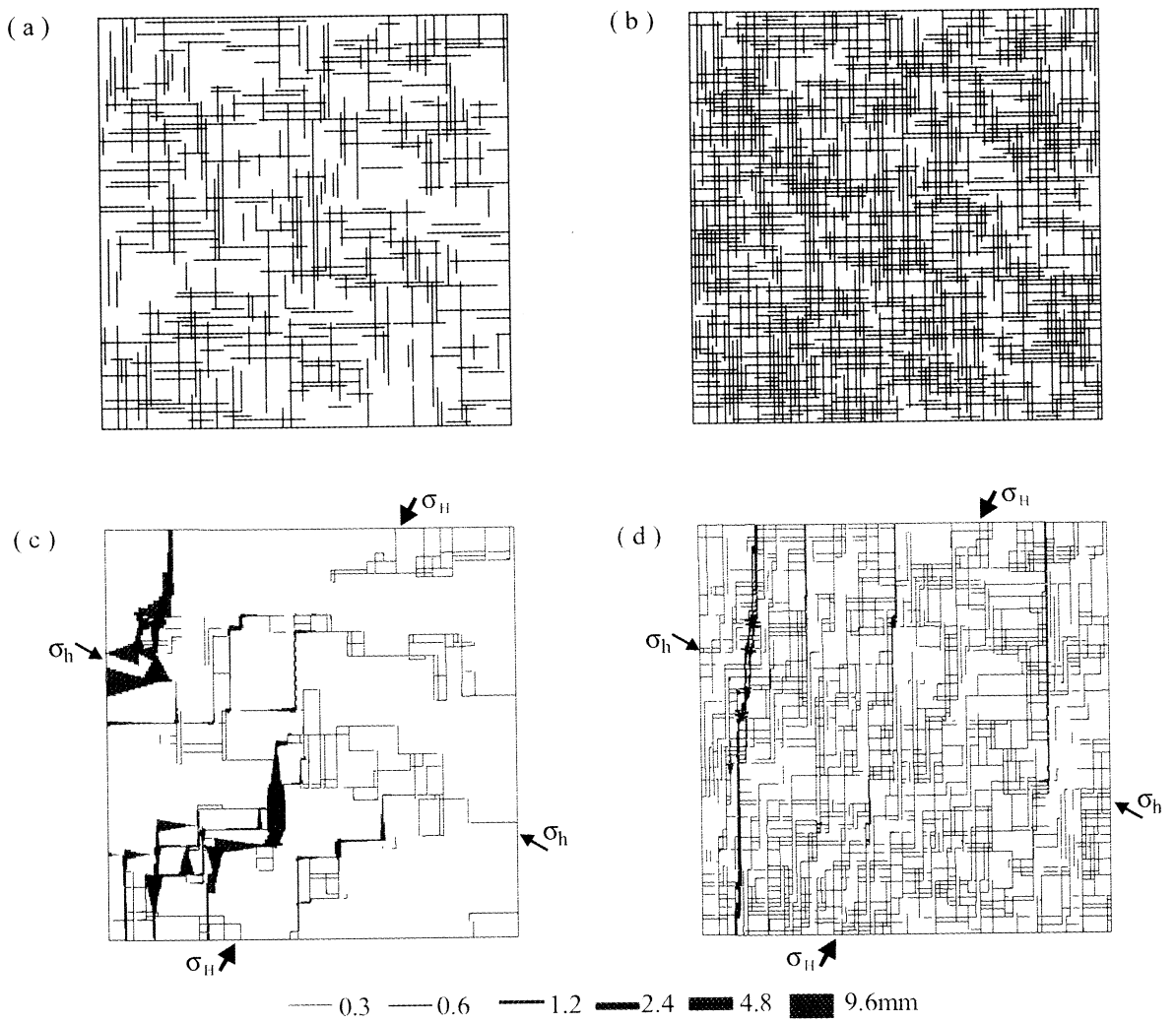

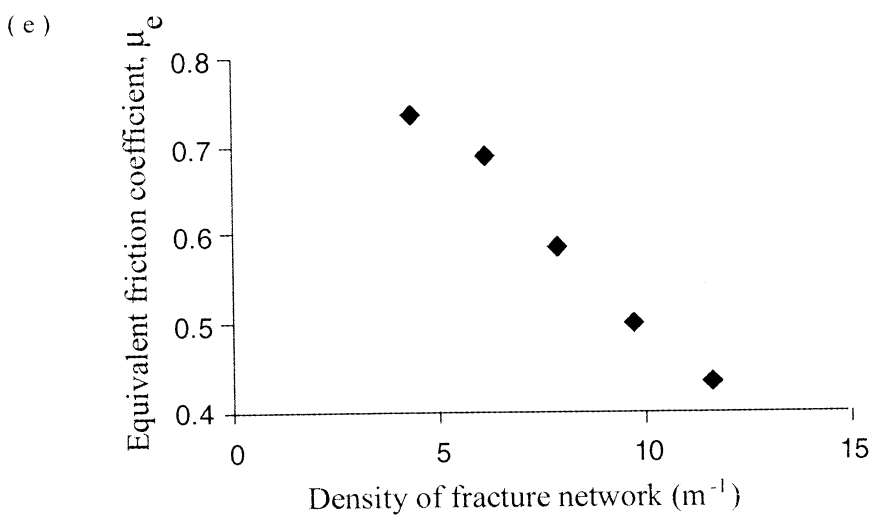

Figure 13. Fracture networks having different densities of between (a) 4.3 m^{-1} and (b) 11.6 m^{-1} with a mean fracture length of 1.15 m. (c) Fracture apertures at critical stress for a fracture density of 4.3 m^{-1} (differential stress of 14.3 MPa, mean stress of 24.05 MPa, and fluid pressure of 16 MPa). (d) Fracture apertures at a higher density of 11.6 m^{-1} (differential stress of 14.3 MPa, mean stress of 24.05 MPa, and fluid pressure of 11.5 MPa). (e) Plot of equivalent frictional strength of fractured rock masses μ_e against fracture density.

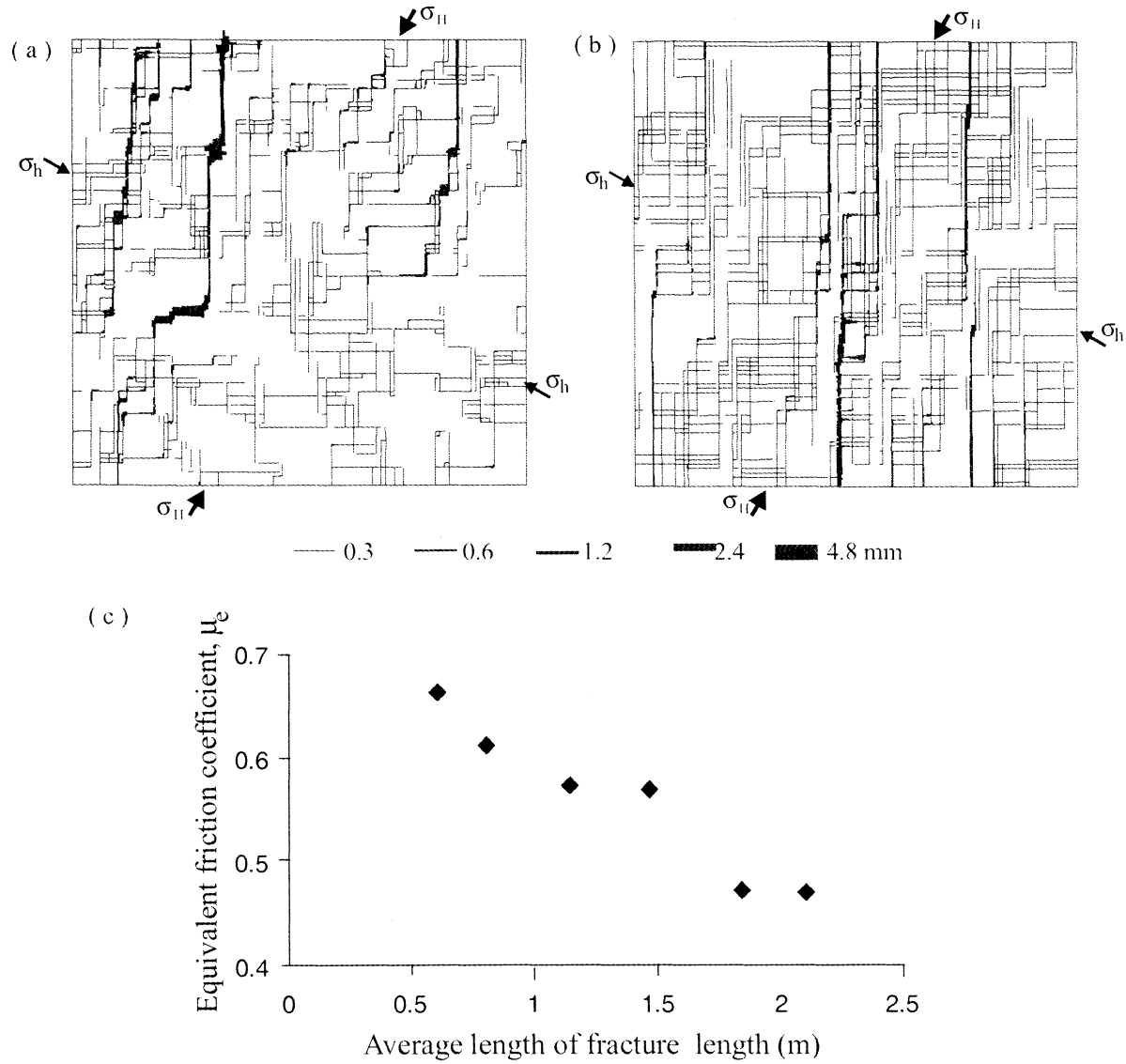

Figure 14. Fracture apertures, at critical stress states, for models with different fracture lengths but same density (7.85 m^{-1}). (a) Short average fracture length (0.61 m) (differential stress of 14.3 MPa, mean stress of 24.05 MPa, and fluid pressure of 14 MPa). (b) Long average fracture length (2.11 m) (differential stress of 14.3 MPa, mean stress of 24.05 MPa, and fluid pressure of 12 MPa). (c) Plot of equivalent frictional strength μ_e against average fracture length.

existence of high anisotropy in fracture networks the process of instability of a system may not be described with a percolation theory because the deformation is strongly localized at an early stage rather than a uniformly dispersed over the entire system, as discussed by *Kolesnikov and Chelidze* [1985].

7. Effects of Loading Direction

To understand the relations between loading direction and fracture orientation, further modeling was carried out for two fracture networks with the same density (7.85 m^{-1}) but different anisotropy coefficients of 1.08 and 3.35. The loading direction (σ_H) was changed at intervals of 15°. For each network, seven different loading directions were tested with three different loading schemes, mading a total of 42 tests.

7.1. Isotropic Fracture Network

At loading directions of 0 and 90° (Figures16a and 16e), the principal stresses are parallel to the fracture sets, and there is little shear displacement along the fractures. In both cases the fluid pressure at the critical state is ~17 MPa, i.e., close to the value of the minor principal stress (16.9 MPa). Note that the fractures have a slightly shorter average length in the 90° direction than at the 0° (anisotropy coefficient of 1.08), which leads to only a small difference in the critical fluid pressure and dilation (see Figures 16a and 16e). For both loading directions, only those fractures that are parallel to the major principal stress open.

Where the principal stress axes are not parallel to the fracture sets, the fluid pressure and differential stress at the criti-

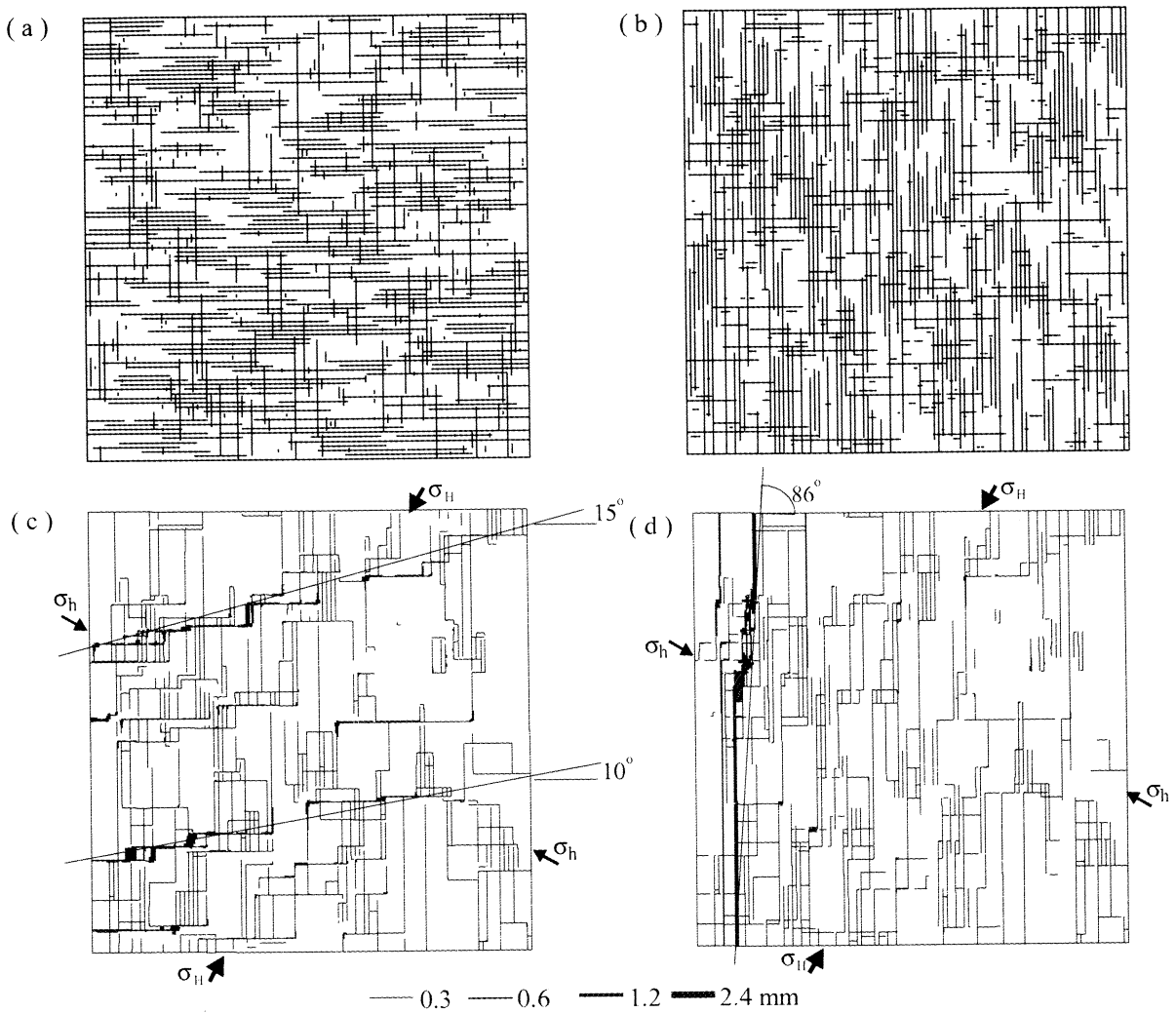

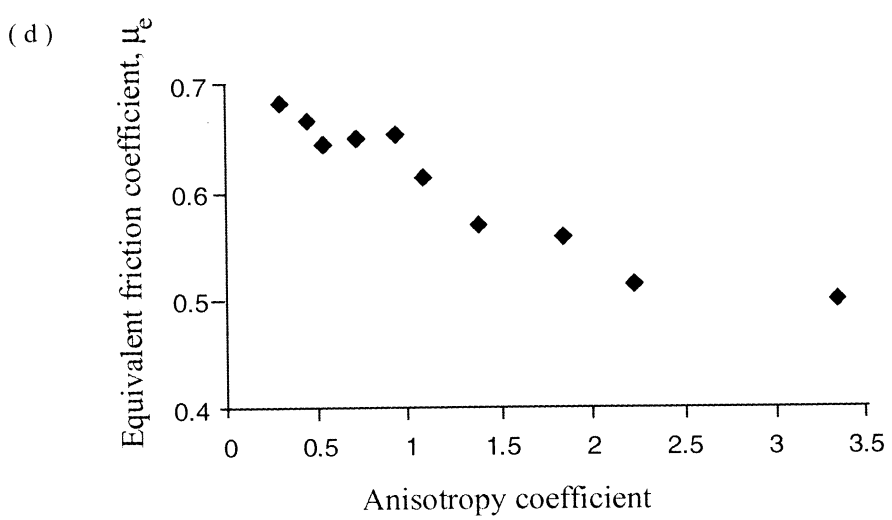

Figure 15. Fractured networks with different anisotropy coefficient between (a) 0.3 and (b) 3.35 but having same fracture density (7.85 m^{-1}). (c) Fracture apertures, at critical stress state, for low anisotropy coefficient of 0.3 (differential stress of 14.3 MPa, mean stress of 24.05 MPa, and fluid pressure of 16 MPa). (d) Fracture apertures, at critical stress state, for high anisotropy coefficient of 3.35 (differential stress of 14.3 MPa, mean stress of 24.05 MPa, and fluid pressure of 11.4 MPa). (e) Plot of equivalent frictional strength μ_e against fracture anisotropy coefficient.

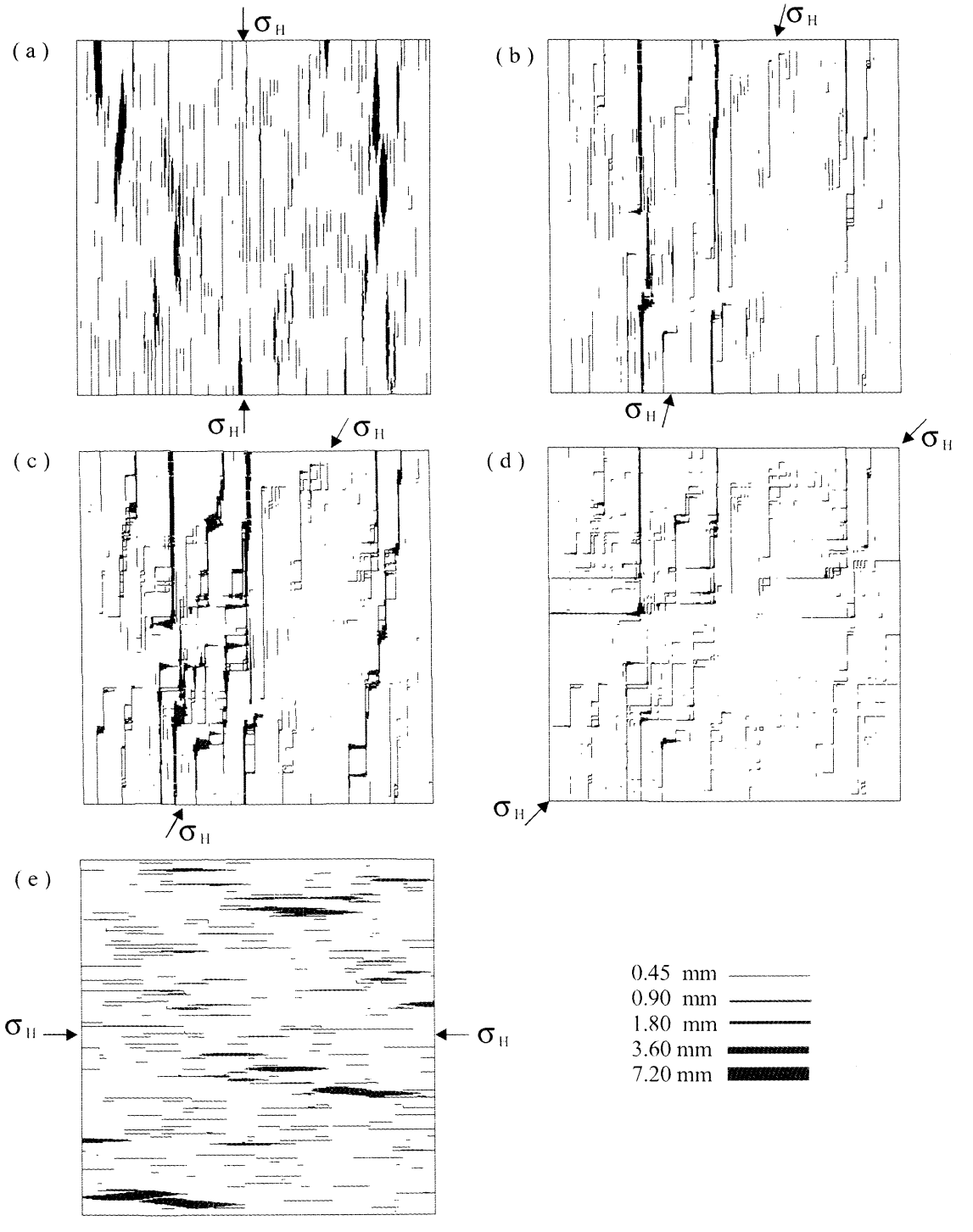

Figure 16. Fracture apertures, at the critical state for different loading directions of the fractured rock mass in Figure 15a (low anisotropy coefficient of 1.08). The loading was performed with scheme 3 with the minor horizontal principal stress of 16.9 MPa and the fluid pressure and the major horizontal principal stress varied at different loading directions. (a) At 0° with critical fluid pressure of 16.8 MPa, σ_H = 81.2 MPa, and fractures opening parallel to the major principal stress. (b) At 15°, with critical fluid pressure of 10 MPa, σ_H = 49.2 MPa, and dilational shearing occuring along some fractures parallel to the major principal stress. (c) At 30°, with critical fluid pressure of 10 MPa, σ_H = 41.2 MPa, and more dilational shearing occuring along some fractures mainly parallel to the major principal stress. (d) At 45°, with critical fluid pressure of 10 MPa, σ_H = 42.2 MPa, and dilational shearing occuring along fractures in both the x and y directions. (e) At 90°, with critical fluid pressure of 17 MPa, σ_H = 91.2 MPa, and fractures opening parallel to the major principal stress.

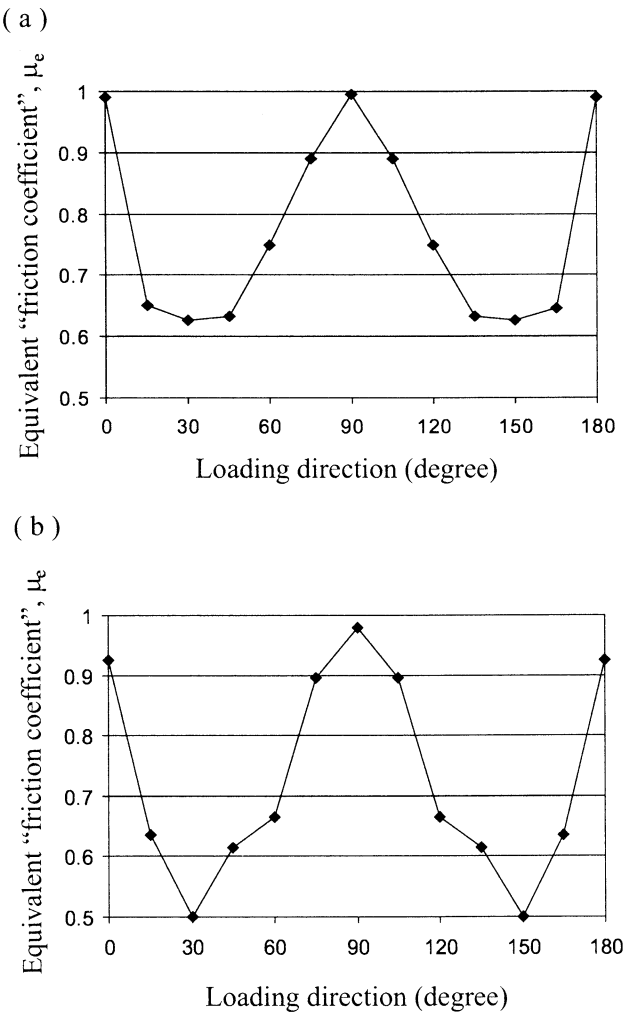

Figure 17. Effects of loading direction on the equivalent friction coefficient, μ_e, for rock masses with (a) low anisotropy (1.08) and (b) high anisotropy (3.35).

cal state are significantly lower, and the deformation patterns are different (Figures16b, 16c and 16d). In these orientations the deformation mainly comprises shearing on the fracture set at the lowest angle to σ_H, linked by dilational jogs utilizing the other fracture set. Where the loading direction bisected the two sets of fractures, dilational shearing occurred along the two sets of fractures, but smaller displacements developed (Figure 16d). In this study with a rotation interval of 15°, the minimum differential stress was 24.3 MPa at a loading direction of 30° (Figure 16c).

The equivalent frictional strength, μ_e, and deformation mode of a fractured rock mass with low anisotropy (1.08) is controlled by the direction of loading (Figure 17a). Similar effects were seen in the modeling of naturally fractured rocks [*Zhang and Sanderson*, 1997; *Sanderson and Zhang*, 1999].

7.2. Anisotropic Fracture Network

The same tests have been applied to a fractured rock mass with a higher anisotropy coefficient of 3.35. The critical stress states are considerably different for the extensional deformation modes (loading at 0 and 90°), and the patterns of extensional deformation are also different. At $S_H = 0°$ (i.e., parallel to the longer fractures) the maximum aperture is relatively small (3.6 mm). At $S_H = 90°$ (parallel to the shorter fractures) the maximum aperture is somewhat large (5.7 mm). Other loading directions produce dilational shear zones, with the anisotropy having a significant influence to the deformation patterns. Where $\sigma_H \leq 45°$, shear zones form along a few long fractures and rock mass is less stable. Where $\sigma_H > 45°$, more shear zones formed, each comprising a number of short fractures linked by dilational jogs, and the fractured rock mass had a higher stability.

The equivalent frictional strength (μ_e) at different loading directions is shown in Figure 17b. Because of the difference in deformation patterns the stability of a highly anisotropic fracture network is very variable at different loading directions. For both extensional and dilational shearing, the stability of the rock mass is lower where the loading direction of the major horizontal principal stress, σ_H, is closer to the longer fracture set.

8. Discussion and Conclusions

The critical stress state at which a fractured rock mass in the upper crust becomes unstable has been investigated using two-dimensional numerical modeling methods. The models involve a connected network of preexisting fractures with no further initiation or growth of fractures. Instability can be triggered by a small change in stress (positive ΔCFS) when the critical stress state is approached. The modeling shows the following features:

1. The critical stress state can be described with reference to a state boundary surface, representing varying differential stress, mean stress, and fluid pressure.

2. An instability strength has been determined from a series of critical stress states obtained under different conditions. The strength of a potential shear zone can be described by a frictional coefficient (μ_z) and a cohesion (C_z), consistent with Mohr-Coulomb theory.

3. The instability strength can also be represented by an equivalent frictional coefficient (μ_e) and an equivalent cohesion (C_e) based on the stresses applied to the rock mass. This approach allows the stability/instability to be determined without knowing the direction of the potential shear zone and hence the shear and normal stresses on it.

4. The stability at a specific stress state can also be defined by a normalized stability factor, which is <1 for stable states and >1 for unstable states.

5. Fracture density has an important effect on instability strength. For fracture densities between 4.3 and 11.6 m^{-1} the equivalent frictional strength (μ_e) varies between 0.74 and 0.44, respectively.

6. Stability decreased with increasing average fracture length. For variation of average fracture length between 0.61 and 2.11 m the equivalent frictional strength (μ_e) changes between 0. 67 and 0.47, respectively.

7. Fracture anisotropy has a considerable effect on the stability; higher anisotropy leads to lower instability strength for a given loading direction. For variation of anisotropy between 0.3 and 3.35 the equivalent frictional strength (μ_e) varies between 0.69 and 0.5, respectively.

8. Loading direction also has a very important impact on the deformation. Where a principal stress is parallel to a fracture set, the deformation is entirely controlled by opening of

those fractures parallel to σ_H. Otherwise, the deformation is characterized by shear zones with sliding, opening and block rotation. There is a direction of loading with σ_H at about $30° \pm 15°$, at which sliding contributes most to the deformation and stability is lowest.

9. Extensional deformation requires the highest driving stress (differential stress or/and fluid pressure). In these cases, the fluid pressure required to open the fractures is very close to the confining stress. For deformation dominated by dilational shearing, the driving stress is much lower.

10. Anisotropy has a considerable effect on stability and the pattern of deformation. For extensional deformation modes a large fluid pressure or large differential stress is required to open fractures. Where $\sigma_H \leq 45°$ to the longer fracture set, the rock mass has a relatively low stability and shear zones consist of a few long fractures. Where $\sigma_H > 45°$ to the longer fracture set, the rock mass has a relatively high stability, and shear zones consist of a number of short fractures, linked by large dilational jogs or pull-aparts.

Rocks that are pervasively fractured show significant variations in strength that are a function of their fracture geometry (density, length, anisotropy) and loading direction. The macroscopic rock strength results from the composite behavior of a system of fractures, with the macroscopic friction coefficient and cohesion of the rock mass differing from that assigned to individual fractures.

Acknowledgments. This work was carried out as part of a NERC micro-to-macro project (grant GST/02/2311). William Powrie and Richard Harkness are thanked for advice and use of computing facilities in the Geomechanics Research Group at the University of Southampton. The authors also thank Patience Cowie, Tamaz Chelidze, and an anonymous reviewer for their constructive comments that have helped to improve the manuscript.

References

Barton, C. A., M. D. Zoback, and D. Moos, Fluid flow along potentially active faults in crystalline rock, *Geology*, *23*, 683-686, 1995.

Benguigui, L., Experimental study of the elastic properties of a percolating system, *Phys. Rev. Lett.*, *53*, 2028-2032, 1984.

Bernaix, J., New laboratory methods of studying the mechanical properties of rocks, *Int. J. Rock Mech., Min. Sci. Geomech. Abstr.*, *6*, 43-90, 1969.

Bro, A., Failure of stepped joints: an analysis and comparison with a measured failure geometry, *Int. J. Rock Mech. Min. Sci. Geomech. Abstr.*, *29*, 179-186, 1992.

Byerlee, J. D., Friction of rocks, *Pure Appl. Geophy.*, *116*, 615-626, 1978.

Chelidze, T. L., Percolation theory as a tool for imitation of fracture process in rocks, *Pure Appl. Geophys.*, *124*, 731-748, 1986.

Cox, S. F., Deformational controls on the dynamics of fluid flow in mesothermal gold systems, in *Fractures, Fluid Flow and Mineralization*, edited by K.J.W. McCaffrey, L. Lonergan, and J.J. Wilkinson, *Geol. Soc. Spec. Publ.*, *155*, 123-140, 1999.

Cundall, P. A., J. Marti, P. Beresford, N. C. Last, and M. Asgain, Computer modelling of jointed rock masses, *WEST Tech. Rep. N-74-8, US Army Engs.*, Vicksburg, Mississippi, 1978.

Das, S., and C. H. Scholz, Theory of time-dependent rupture of the Earth, *J. Geophys. Res.*, *86*, 6039-6051, 1981.

Dershowitz, W. S., and H. H. Einstein, Characterising rock joint geometry with joint system models, *Rock Mech. Rock Eng.*, *21*, 21-51, 1988.

Einstein, H. H., D. Veneziano, G. B. Baecher, and K.J. O'Reilly, The effects of discontinuity persistence on rock slope stability, *Int. J. Rock Mech. Min. Sci. Geomech. Abstr. 20*, 227-236, 1983.

Gerrard, C., Shear failure of rock joints: appropriate constrains for empirical relations, *Int. J. Rock Mech. Min. Sci. Geomech. Abstr.*, *23*, 421-9, 1986.

Harper, T. R., and N. C. Last, Response of fractured rock subject to fluid injection, part II, Characteristic behaviour, *Tectonophysics*, *172*, 33-51, 1990.

Harris, R. A., Introduction to special section: Stress triggers, stress shadows, and implications for seismic hazard, *J. Geophys. Res.*, *103*, 24,347-24,358, 1998.

Healy, J. H., W. W. Rubey, D. T. Griggs, and C. B. Raleigh, The Denver earthquakes, *Science, 161*, 1301-1310, 1968.

Hoek, E., and E. T. Brown, *Underground Excavation in Rock*, 1st Edition, Inst. of Min. and Metall., London, 1980.

Hudson, J. A., The understanding of measured changes in rock structures, in situ stress and water flow caused by underground excavation, paper presented at 2nd International Symposium On Field Measurements in Geomechanics, Japan Society of Civil Engineers, Kobe, Japan, 1987.

Hung, J. J., and T. T. Lee, A study of the shear strength of rock joint of partial continuity, in *Rock Joints*, edited by N. Barton and O. Stephansson, pp. 219-225, A. A. Balkema, Brookfield, Vt., 1990.

Jaeger, J. G., and N. G. W. Cook, *Fundamentals of Rock Mechanics*, 3rd ed. Chapman and Hall, New York, 1979.

Kolesnikov, M., and T. L. Chelidze, The anisotropic correlation in percolation theory, *J. Phys. A: Math. Gen.*, *18*, L273-L275, 1985.

Lajtai, E. Z., Strength of discontinuous rocks in shear, *Geotechnique*, *19*, 218-33, 1969.

Patterson, M., *Experimental Rock Deformation*, 254 pp. Springer-Verlag, New York, 1978.

Pusch, R., Alternation of hydraulic conductivity of rock by tunnel excavation, *Int. J. Rock Mech. Min. Sci. Geomech. Abstr.*, *26*, 79-83, 1989.

Raleigh, C. B., J. H. Healy, and J. D. Bredehoeft, An experiment in earthquake control at Rangely, Colorado, *Science, 191*, 1230-1237, 1976.

Reasenberg, P. A., and R. W. Simpson, Response of regional seismicity to the static stress change produced by the Loma Prieta earthquake, *Science*, *255*, 1687-1690, 1992.

Reuschle, T., A network approach to fractures: The effect of heterogeneity and loading conditions, *Pure and Appl. Geophys.*, *152*, 641-665, 1998.

Rummel, F., G. Mohring-Erdmann, and J. Baumartner, Stress constraints and hydrofracturing stress data for the continental crust, *Pure Appl. Geophys.*, *124*, 875-892, 1986.

Sanderson, D. J., and X. Zhang, Critical stress localization of flow associated with deformation of well-fractured rock masses, with implications for mineral deposits, in *Fractures, Fluid Flow and Mineralization*, edited by K.J.W. McCaffrey, L. Lonergan, and J.J. Wilkinson, *Geol. Soc. Spec. Publ.*, *155*, 69-81, 1999.

Sanderson, D. J., and X. Zhang, Numerical analysis of instability and associated localization of deformation and fluid flow in fractured rocks, *J. Struc. Geol.* in press, 2001.

Santarelli, F. J., D. Dahen, H. Baroudi, and K. B. Sliman, Mechanisms of borehole instability in heavily fractured rock media, *Int. J. Rock Mech. Min. Sci. Geomech. Abstr.*, *29*, 457-467, 1992.

Scholz, C. H., *The Mechanics of Earthquakes and Faulting*, Cambridge Univ. Press, New York, 1990.

Spicak, A., T. Lokajicek, and L. Waniek, Seismic regime of a single fault model, *Pure Appl. Geophys.*, *124*, 788-810, 1986.

Stauffer, D. and A. Aharony, *Introduction to Percolation Theory*, Taylor and Francis, Philadelphia, Pa., 1991.

Talwani, P., and S. Acree, Pore pressure diffusion and the mechanism of reservoir-induced seismicity, *Pure Appl. Geophys.*, *122*, 947-965, 1985.

Toda, S., R. S. Stein, P. R. Reasenberg, J. H. Dieterich, and A. Yoshida, Stress transferred by the 1995 M_w = 6.9 Kobe, Japan, shock: Effect on aftershocks and future earthquake probabilities, *J. Geophys. Res.*, *103*, 24,373-24,358, 1998.

Vlokh, N. P., A. V. Zoubkov, and Y. P. Shoupletsov, Determination of stresses and strain modulus in a rock mass by experimental-analytical method, paper presented at 2nd International Symposium On Field Measurements in Geomechanics, Japan Society of Civil Engineers, Kobe, Japan, 1987.

Vlokh, N. P., A. V. Kritikov, and Y. P. Shoupletsov, In-situ study of strength and strain characteristics of a rock mass based on sign-variable deformations in a pillar, in Rock Joints, edited by N. Barton and O. Stephansson, pp. 335-339, A. A. Balkema, Brookfield, Vt., 1990.

Zhang, S., S. F. Cox, and M. S. Patterson, The influence of room

temperature deformation on porosity and permeability in calcite aggregates, *J. Geophys. Res.*, *99*, 15,761-15,775, 1994.

Zhang, X., Shear resistance of jointed rock masses and stability calculation of rock slopes, *Geotech. Geol. Eng.*, *11*, 107-124, 1993.

Zhang, X., and D. J. Sanderson, Fractal structure and deformation of fractured rock masses, in *Fractal and Dynamic Systems in Geoscience*, edited by J.H. Kruhl, 00. 37-52, Springer-Verlag, New York, 1994.

Zhang, X., and D. J. Sanderson, Anisotropic features of geometry and permeability in fractured rock masses, *Eng. Geol., 40*, 65-75, 1995.

Zhang, X., and D. J. Sanderson, Effects of loading direction on localized flow in fractured rocks, in *Computer Methods and Advances in Geomechanics*, edited by J. X. Yuan, pp. 1027-1032, A. A. Balkema, Brookfield, Vt., 1997.

Zhang, X., and D. J. Sanderson, Numerical study of critical behaviour of deformation and permeability of fractured rock masses, *Mar. Pet.. Geol., 15*, 535-548, 1998.

Zhang, X., N. C. Last, W. Powrie, and R. Harkness, Numerical modelling of wellbore behaviour in fractured rock masses, *J. Pet. Sci. Eng., 23*, 95-115, 1999a.

Zhang, X., W. Powrie, R. Harkness, and S. Wang, Estimation of permeability for the rock mass around the shiplocks of the Three Gorges Project, China, *Int. J. Rock Mech. Min. Sci. Geomech. Abstr., 36*, 381-397, 1999b.

Zoback, M., C. Barton, T. Finkbeiner, and S. Dholakia, Evidence for fluid flow along critically-stresses faults in crystalline and sedimentary rock, in *Faulting, Fault Sealing and Fluid Flow in Hydrocarbon Reservoirs, edited by* G. Jones, Q. Fisher, and R. Knipe, pp. 47-48, Univ. of Leeds, Leeds, England, 1996.

D. J. Sanderson and X. Zhang, T. H. Huxley School of Environment, Earth Sciences and Engineering, Imperial College of Sciences, Technology and Medicines, London, SW7 2BP, England, UK. (david.sanderson@ic.ac.uk; x.zhang@ic.ac.uk)

(Received June 8, 2000; revised December 5, 2000;
accepted March 14, 2001.)